Semi-Implantable Wireless Power Transfer (WPT) System Integrated With On-Chip Power Management Unit (PMU) for Neuromodulation Application

Dipon K. Biswas , Nabanita Saha, Arnav Kaul , and Ifana Mahbub , Senior Member, IEEE

Abstract—Miniaturization of the neuromodulation system is important for non-invasive or sub-invasive optogenetic application. This work presents an optimized wireless power transfer (WPT) system integrated with an on-chip rectification circuitry and an off-chip stimulation circuitry for optogenetic stimulation of freely moving rodents. The proposed WPT system is built using parallel transmitter (TX) coils on printed circuit board (PCB) and wirewound based receiver (RX) coil followed by a seven-stage voltage doubler and a low dropout regulator (LDO) circuit designed in 180 nm standard Complementary Metal Oxide Semiconductor (CMOS) process. A pulse stimulation is used to stimulate the neurons which is generated using a commercially available off-theshelf (COTS) components based oscillator circuit. The intensity of the stimulation is controlled by using a COTS based LED driver circuit which controls the current through the μLED . The total dimension of the RX coil is 8 mm imes 3.4 mm. The maximum power transfer efficiency (PTE) of the proposed WPT system is \sim 35% and the power conversion efficiency (PCE) of the rectifier is 52%. The proposed system with reconfigurable stimulation frequency is suitable for exciting different brain areas for long-term health monitoring.

Index Terms—Duty-cycled stimulation, optogenetic, CMOS, wireless power transfer, power transfer efficiency.

I. INTRODUCTION

E LECTRONIC, optoelectronic, and microfluidic inter-faces with living biosystems have advanced to the point where adaptable devices capable of interrogating and altering the behavior of the central and peripheral nervous systems may now be built [1], [2]. Advances in neuroengineering makes it easier to create long-lasting neural interfaces with a variety of operational modes and integration methods in freely moving animals.

Optical fiber technologies developed from those used in the telecommunications industry, for example, are commonly utilized in optogenetic stimulation and photometric recordings for

Manuscript received 10 November 2022; revised 23 February 2023; accepted 5 March 2023. Date of publication 27 March 2023; date of current version 31 May 2023. This work was supported by the National Science Foundation (NSF) under Grant ECCS 2309413.

Dipon K. Biswas is with the Department of Electrical Engineering, University of North Texas, Denton, TX 76207 USA (e-mail: diponkumar-biswas@my.unt.edu).

Nabanita Saha and Ifana Mahbub are with the Electrical and Computer Engineering, The University of Texas at Dallas, Richardson, TX 75080 USA (e-mail: nabanita.saha@utdallas.edu; ifana.mahbub@utdallas.edu).

Arnav Kaul is with the Frisco Independent School District, Frisco, TX 75035 USA (e-mail: arnaykaul5@gmail.com).

Digital Object Identifier 10.1109/JERM.2023.3256705

analyzing the neural function in the brain [3], [4]. However, tethered technologies present special challenges when interfacing with highly mobile body areas such as the spinal cord and peripheral nerves because fixation to mechanical anatomy parts like the skull is required [5]. Moreover, the forces due to plugging, unplugging, and unwinding of the probes from the implanted device can cause tissue damage which may result in chronic instability [6].

Electrochemical power sources like batteries and supercapacitors are used in optogenetic stimulation to avoid the problems due to tethered technologies [7], [8]. Rigid printed circuit boards are commonly used as mounting sites for centimeter-scale electronic components for transferring data wirelessly, physiological recording, and stimulation control. Devices that utilize these designs, on the other hand, might cause discomfort, and infections, as well as limit the small animals to move freely. The size and weight of these devices are the main limiting factors [9], [10]. For comprehensive and long-term implantation, fully wireless and lightweight devices that are battery-free and adopt millimeter-scale dimensions offer ongoing behavioral investigations without the requirement for human contacts that can affect natural behaviors. In [11], a safe and suitable WPT system for small-sized, deep-body implants is proposed but the PTE is low (0.67%) compared to the proposed work. The efficiency of far-field transmission depends on the angle between the transmitter (TX) and receiver (RX) coils. Moreover, the efficiency decreases significantly as the distance increases. The near-field inductive coupling has better efficiency within the same distance. For wireless acquisition of brain signals, the DC voltage is provided via an infrared-illuminated photovoltaic cell in [12]. The advantage of using implanted infrared receiver instead of visible light is it provides improved skin penetration. But the PTE is only 15% which is much lower than the proposed system. Inductively-coupled wireless power transfer systems have been developed to meet the challenge of higher power transfer efficiency in experiments with freely-moving animals. However, the PTE is not that high with respect to the powering distance [13]. Head-mounted wireless receivers are desirable for enabling optogenetic neural stimulation [14]. In this paper, a near-field magnetic resonant coupling method is used to transfer power to the implantable device and obtain higher PTE.

Fig. 1 represents the overview of the conventional neuromodulation system for optogenetic application. The RX coil

2469-7249 © 2023 IEEE. Personal use is permitted, but republication/redistribution requires IEEE permission. See https://www.ieee.org/publications/rights/index.html for more information.

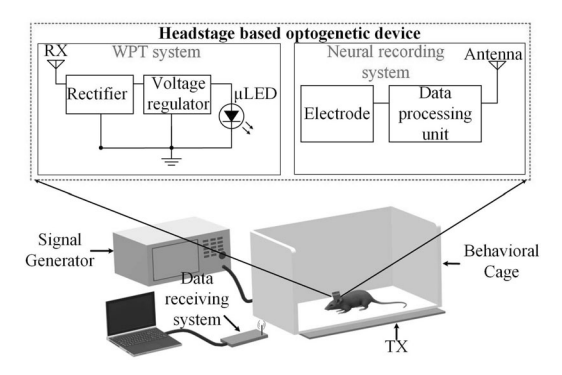


Fig. 1. Overview of the conventional neuromodulation system for freely moving animal.

is designed to be mounted on the headstage of the freely moving rats inside a behavioral cage. The miniaturization of the implantable system is required to cause minimal hindrance during the optogenetic stimulation of freely moving animals. The rectification circuit which includes a rectifier [15], and voltage regulator circuit can be realized on a CMOS chip. An active-voltage doubling rectifier is presented in [16]. However, the input decoupling capacitor and output coupling capacitor are realized off-chip which increase the form factor of the implant. A voltage regulator circuit such as a DC-DC converter or a low dropout (LDO) is required in a WPT system along with the rectifier to regulate the voltage at the load [17]. The WPT system is delivering power not only to the μ LED But also the recording system. The voltage regulator output goes to the Vdd (supply voltage) of the data processing unit. The connection between the WPT output and the data processing unit's supply is wired.

The next block of the semi-implantable wirelessly powered optogenetic system is the pulse stimulation circuit for neural stimulation. The stimulation parameters include several degrees of freedom, each of which is tailored to a specific application. The stimulation frequency, pulse width, and output voltage delivered to the LED are all part of the parameter set [18]. Changing the stimulation parameters improves the efficacy of the stimulation and the clinical outcomes. For example, lowfrequency stimulation (<100 Hz) improves the efficacy of deep brain stimulation, whereas severe gait disorder can be treated with high-frequency stimulation (130-185 Hz) [19]. In prior works, multiple resonators are proposed to enhance PTE, but that increases the chance of detuning and thus results in a reduced PTE [20], [21], [22]. The objective of the work is to use only a single RX and eliminate the need of using multiple resonators to avoid complexity.

The contributions of this work are: 1) the design of an optimized TX-RX coil based WPT system integrated with an on-chip rectifier and LDO circuit where the RX coil is miniaturized for achieving the optimum PTE, 2) an off-chip based stimulation circuit having reconfigurable stimulation frequencies (10–50 Hz) for optogenetic applications, and 3) avoiding the use of resonators. The paper is structured as follows: Section II discusses the detailed design architecture of the WPT system, rectification circuitry, and stimulation circuit. The simulation

and experimental validation are provided in Section III, followed by a conclusion in Section IV.

II. SYSTEM OVERVIEW

The proposed wirelessly powered neuromodulation system includes two parallel transmitter (TX) coils, implantable receiver (RX) coil, on-chip power management unit (PMU), and neural stimulation circuit as shown in Fig. 2. Off-chip components are used as prototypes. The proposed TX coils are attached to the signal generator through a matching network and a commercially available SMAKN 2 MHz-700 MHz RF power amplifier with a gain of 15 dB. The TX coils, TX_1 and TX_2 are modeled as an RLC circuit denoted by L_{TX1} , R_{TX1} , and C_{TX1} , and L_{TX2} , R_{TX2} , and C_{TX2} , respectively. The proposed implantable receiver coil is also modeled as an RLC circuit denoted as L_{RX} , R_{RX} , and C_{RX} . The RX coil is followed by a matching network that is used to match the impedance of the RX coil with the impedance of the PMU and the neural stimulation circuit. The PMU consists of a rectifier and an LDO circuit designed using 180 nm CMOS process. The final stage of the proposed system is a neural stimulation circuit consisting of a COTS based oscillator, an LED driver circuit, and a μ LED. An LB-QH9G μ LED by OSRAM Opto-semiconductors which has a power requirements of 13.5 mW with a forward voltage of 2.7 V and a minimum forward current of 5 mA is used as light stimulation source for neuromodulation experiments.

The whole headstage system is powered by a power management unit (PMU) which consists of a Lithium-ion battery, a low-dropout regulator (LDO), providing 3.3 V to the neural analog front-end (AFE), the transceiver, and the neural stimulation circuit. An μ LED is used as the optical stimulation source which is driven by a pulse signal from an oscillator to stimulate the neural cells. The oscillator generates a 20% duty-cycled pulsed signal at a reconfigurable frequency range of 10–50 Hz with a supply voltage of 3.3 V from the LDO.

A. Wireless Power Transfer System

1) Coil Optimization: The proposed WPT system is designed based on the inductive coupling method. An optimization technique is followed for modeling the spiral TX coil and the wire-wound RX coil [23]. Prior to the optimization process, several parameters are needed to be discussed. The representative unit cell of the TX coil design is shown in Fig. 3(a) where d_o is the outer diameter, d_i is the inner diameter, ϕ is the fill ratio, w is the trace width, and s is the trace spacing. The fill ratio of a spiral coil is a function of outer diameter and inner diameter of the coil as represented in (1).

$$\phi = \frac{d_o - d_i}{d_o + d_i} \tag{1}$$

Fig. 3(b) illustrates the dimension for the wire-wound RX coil where w_{rx} and d indicate the width and diameter of the wire-wound coil, respectively.

The optimization process for modeling the TX and RX coils is shown in Fig. 4. The proposed optimization process starts with selecting the initial dimensions of the TX and RX coils based on

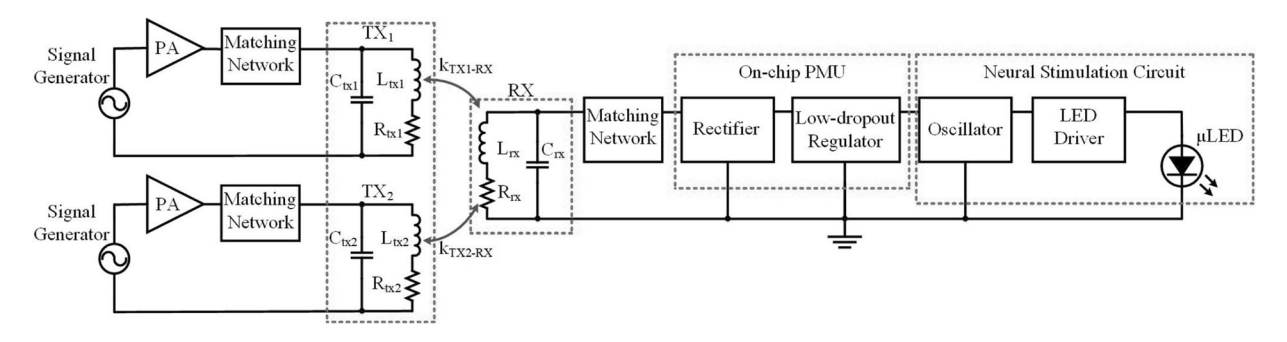


Fig. 2. System-level diagram of the proposed wireless neuromodulation system.

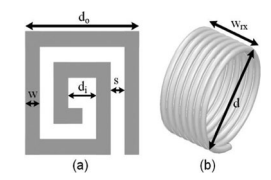


Fig. 3. Representative figure of (a) Spiral TX coil dimension, and (b) Wirewound based RX coil dimension.

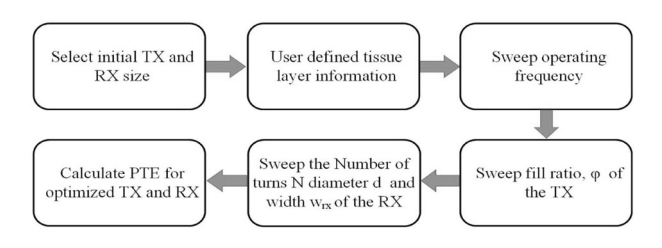


Fig. 4. Optimization process for modeling the TX and RX coils.

the design and fabrication constraints. The behavioral cage that is used in this experiment has a total dimension of 215 mm \times 215 mm. To reduce the processing time of the optimization, a TX coil array is designed for this work having sixteen TX unit cells having 50 mm \times 50 mm dimension, as illustrated in Fig. 6(a). Due to the size restriction of the implantable RX coil and the size of the rat's brain, the diameter of the RX coil cannot exceed 4 mm diameter and the width cannot be more than 10 mm [24]. Thus, in the first step of the optimization, the outer diameter d_0 of the TX coil is set to 50 mm and the maximum diameter d of the RX coil is chosen as 3 mm as shown in Fig. 3. In the next step, the tissue layer (such as skin, skull, and greymatter) information, such as thickness, relative permittivity ϵ_r , and conductivity σ are defined in the optimization [25].

In the next step, the operating frequency is swept from 1 MHz to 30 MHz to select the best design in terms of PTE. The fourth step starts sweeping the fill ratio ϕ of the TX coil followed by the sweeping of d and w_{rx} of the RX coil in the fifth step. In the final step, the dimension of the optimized TX and RX coils are finalized for the maximum achievable PTE. The optimization code is written using Python language. The number of turns of the TX coil is varied from 2-turns to 3-turns while the diameter of the TX is kept constant to 50 mm \times 50 mm and the number

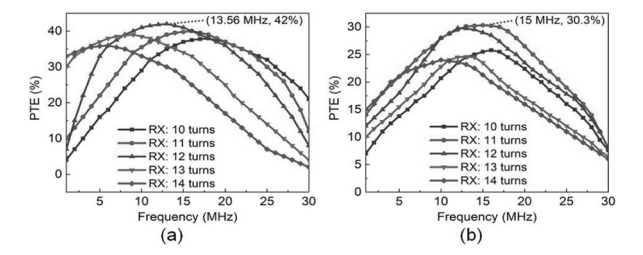


Fig. 5. Optimized PTE for several RX coils, when (a) the TX coil unit cell is $50~\text{mm} \times 50~\text{mm}$ with two turns, and (b) the TX coil unit cell is $50~\text{mm} \times 50~\text{mm}$ with three turns.

of turns of the RX coil is swept from 10-turns to 14-turns. The maximum PTE is found to be 42% at 13.56 MHz while the TX coil has 2-turns and the RX coil has 12-turns as shown in Fig. 5(a). The number of turns of the RX coil is varied from 10 to 14 turns while the frequency is varied from 1 to 30 MHz keeping the number of turn of the TX coil unit cell to 3. The number of turns of the TX coil is increased to 3 turns. As illustrated in Fig. 5(b), the maximum PTE is achieved as 30.3% at 15 MHz frequency for this condition while the RX coil has 11 turns. Thus, the proposed RX coil is chosen to have 12 turns and the TX coil is chosen to be 50 mm × 50 mm with 2 turns operating at 13.56 MHz. For the same TX and RX coils different frequencies will yield different PTE/PCE. The resonating capacitors need to be changed to change the resonating frequency.

2) Transmitter Coil Architecture: Based on the optimization technique mentioned above, the unit cell of the TX coil with a dimension of 50 mm \times 50 mm are obtained as shown in Fig. 6(a). The unit cell is a 2-turns planer square coil with a trace width/spacing of 5 mm. To distribute the power across the total area of the behavioral cage of the freely moving rodent, the total dimension is set to be 215 mm imes 215 mm. The TX coil board designed to be placed underneath the cage. The TX coil board is divided into two parallel TX coil arrays TX_1 and TX_2 , where each coil consists of eight TX coils connected in series. If the TX coil arrays were connected in series, the Q-factor would be reduced, and the overall efficiency of the system would be reduced as well. The proposed WPT system employs parallel TX coils with parallel feeding networks, which reduces overall resistance and improves the Q-factor, thereby improving the magnetic field. The feeding network includes a

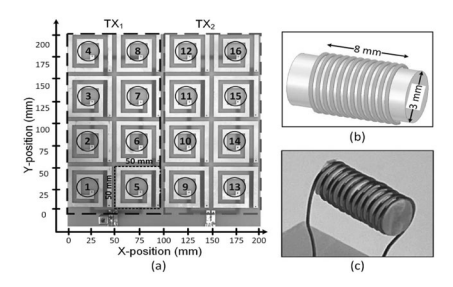


Fig. 6. (a) Fabricated transmitter array on PCB. (b) Simulated wire-wound based RX coil. (c) Fabricated RX coil.

2:1 power divider to supply power to the two parallel TX coil arrays. The TX coils connection follows the Curl right-hand rule so that the current flowing through the unit cell is in the opposite direction for the adjacent unit cells which enhances the magnetic field [26]. Both TX_1 and TX_2 are connected to two separate external signal generators through two power amplifiers (PAs) (SMAKN 2MHz-700 MHz, 3 W amplifier) with a 15 dB gain and a bias voltage of 8.5 V. A combiner is supposed to be designed in future so that the PAs can be driven by a single signal generator. The input impedance of the TX coils are matched with the input impedance of the PA using an L-shape matching network for each TX coil. The L-shape matching network consists of a 42 nH inductor and a 3300 pF capacitor. A resonating capacitor of 82 pF is used to resonate the TX coil to 13.56 MHz, which is within the ISM frequency band.

3) Receiver Coil Architecture: The optimized RX coil is a wire-wound coil based antenna with 12 turns. A 32 AWG remington wire is used to fabricate the RX coil which has a wire diameter of 0.4 mm. The wire is wrapped around a 3 mm diameter cylinder made with PLA (Polylactic acid) which makes the outer diameter of the RX coil to be 3.4 mm with 8 mm total length. The fabricated RX coil is also designed and simulated in HFSS. The simulated and fabricated RX coil architecture is shown in Fig. 6(b) and (c), respectively. To resonate the RX coil to 13.56 MHz frequency, a resonating capacitor with a value of 864 pF is used in parallel with the RX coil is followed by a matching network for matching the impedance of the load circuitry which are the PMU and the neural stimulation circuit in this work.

B. Power Management Unit

The RX coil is connected to the PMU which consists of a seven-stage voltage doubler and a low dropout regulator (LDO) designed in 180 nm CMOS process. The designed chip for the rectifier and voltage regulators are implantable.

1) Rectifier: A seven-stage schottky diode based voltage doubler is proposed as a rectifier circuit and designed in 180 nm CMOS process [27]. The number of stages increases the output voltage level of the rectifier circuit. However, the number stages cannot be increased infinitely as the power dissipation also increases with the introduction of each stages. Thus, in this work a trade-off between the output DC voltage and power dissipation has been found in seven-stage voltage doubler circuit.

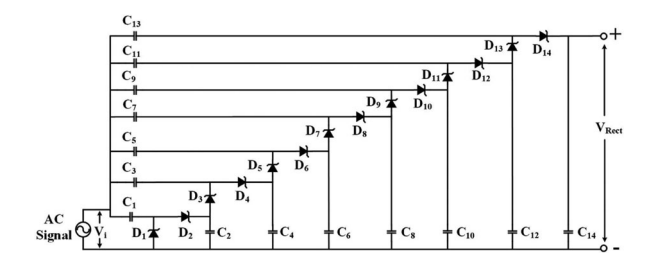


Fig. 7. Schematic of the proposed seven-stage voltage doubler.

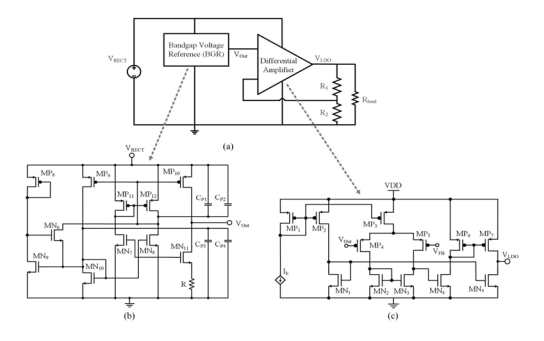


Fig. 8. Schematic of the proposed LDO circuit along with a Band Gap Voltage Reference (BGR) circuit and a differential amplifier.

The schottky diode has a low forward voltage requirements of 150 mV [28]. As shown in Fig. 7, the first stage of the voltage doubler consists of two diodes D_1 and D_2 . The capacitors C_1 and C_2 are the input and output capacitors, respectively which are used to transfer charge from one stage to the next stage. A 10 pF and a 100 pF on-chip capacitors are used as the input and output capacitors, respectively for each voltage doubler stage. The rectifier circuit presented in this work has seven stages. The number of stages enhances the output voltage level of the rectifier circuit. However, the number stages cannot be increased infinitely as the power dissipation also increases with the introduction of each stages. Thus, in this work the trade-off between the output DC voltage and the power dissipation of each rectifier stage has been assessed, and it is found that seven is the optimum number of stages that yields the highest power conversion efficiency (PCE) [27]. The total layout dimension of the on-chip voltage doubler circuit is 300 μ m \times 90 μ m.

Diode D_1 is forward biased and C_1 is charged to V_i during the input signal's negative half-cycle. In the positive half-cycle of the input signal, C_1 is charged to $2V_i$, as it cannot be discharged through D_1 . As a result, D_2 is turned on and consequently C_2 is charged to $2V_i$. In the next negative half-cycle, D_3 turns on and C_3 is charged to $3V_i$. Again, C_3 is charged to $4V_i$, turning on D_4 and charging C_4 to $4V_i$ in the positive half-cycle. Thus the same method applies to all the succeeding stages of the rectifier [29].

2) Low-Dropout Regulator: The proposed LDO circuit consists of a bandgap voltage reference (BGR) and a differential amplifier as represented in Fig. 8(a). To control the output voltage of the LDO, a resistive divider consisting of R_1 and R_2 is used at the output. R_{load} is used as the load that is emulated by stimulation circuit. The value of the resistive dividers can be chosen based on the required output voltage using (2), where

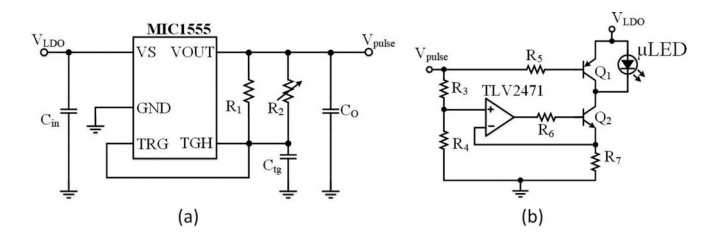


Fig. 9. (a) Schematic of the MIC1555 timer circuit. (b) Schematic of the LED driver circuit.

 V_{FB} is the feedback voltage.

$$V_{LDO} = V_{FB} \times \left(1 + \frac{R_1}{R_2}\right) \tag{2}$$

To achieve a voltage output, V_{LDO} of 3.3 V, in this work, 25 k Ω and 13.48 k Ω resistors are used as R_1 and R_2 , respectively which results in a feedback voltage, V_{FB} of 0.5 V.

The proposed differential amplifier consists of a differential gain stage along with a current mirror circuit to convert the differential input to single-ended output as shown in Fig. 8(c). Transistor MP_4 , MP_5 , MN_2 , and MN_3 form the differential gain stage of the amplifier. The gate of transistor MP_4 is the non-inverting input and the gate of transistor MP_5 is the inverting input. The differential input is amplified according to the gain of differential stage. The gain of the differential stage is the transconductance of MP_4 times the total output resistance seen at the drain of MP_5 . The current mirror circuit is formed by MN_2 and MN_3 . A biasing network is also designed using transistor MP_1 and a reference current source of 5 μ A is used as the bias current, I_b . The biasing network provides a voltage at the gate of the MP_2 and MP_3 which are designed to be in saturation region.

III. IMPLEMENTATION AND MEASUREMENT RESULTS

A. Neural Stimulation Circuit

The PMU circuit is followed by a neural stimulation circuit which includes an oscillation circuit and an LED driver circuit along with a μ LED. Based on the target brain areas, the turn-on/turn-off frequency of the μ LED is varied. In this work, a commercially available MIC1555 CMOS RC oscillator by Microchip is used to provide pulse signal to the μ LED as illustrated in Fig. 9(a). The supply voltage of the oscillator varies from 2.7 V to 18 V which are fed through an input capacitor of 1 μ F to decouple the input signal noise. The oscillator circuit is a SOT-23 packaged chip which can be used as a monostable or as an astable oscillator. In this work, the astable mode of the oscillator is used to provide a constant pulse signal for stimulation. During the astable mode, the threshold (THG) and trigger (TRG) pin are shorted as shown in Fig. 9(a). The output frequency of the oscillator in a stable mode can be reconfigured according to the (3).

$$f = \frac{1}{k_1 RC} \tag{3}$$

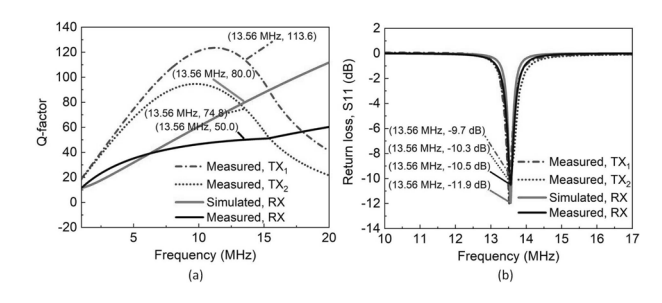


Fig. 10. (a) Q-factor of the proposed TX and RX coils. (b) Return loss of the proposed TX and RX coils.

The non-inverting input signal of the differential amplifier is provided from the output of the BGR. The conventional BGR circuit is composed of an operational amplifier, capacitors, and resistor as shown in Fig. 8(b). The output voltage of the BGR can be calculated according to (4) where the I_{MN11} is the current through transistor MN_{11} and R is the resistance with 1 k Ω .

$$V_{Out} = I_{MN11}R \tag{4}$$

 k_1 is a constant which has a constant value of 1.42 for the RC constant range of 0.01–0.1 s. In this work, a fixed resistance of 220 $k\Omega$ is used as R_1 resistance and a 1 μ F capacitor is used as a threshold capacitor. To make the oscillator reconfigurable for 10–50 Hz frequency, a variable resistor R_2 having a resistance range of 10 $k\Omega$ -110 $k\Omega$ is used, and a load capacitor C_o of 100 pF is used to make the output pulse smoother. In the future, a digitally programmable resistor (such as a 4-bit resistor) will be used to switch the values of the resistor. By using a bi-directional communication method, it will be possible to change the value of the variable resistor after the implantation of the system.

The output signal of the oscillator circuit is used as an input to an LED driver circuit to drive the μ LED in a duty-cycled fashion. The LED driver circuit is used to regulate the current through the μ LED which eventually controls the intensity of the light stimulation. The LED driver used in this work are designed using commercially available components such as a closed-loop op-amp, TLV2471 by Texas Instruments, NPN (BC817) and PNP (BC857) Bipolar Junction Transistors (BJTs) denoted by Q_1 and Q_2 , and resistors as shown in Fig. 9(b). A fixed voltage to the emitter of Q_2 is provided by the op-amp based current source. Thus, the current through the precision resistor R_7 is also guaranteed. As a result, the current through the μ LED is also maintained which is connected in parallel to the Q_1 transistor.

B. WPT System

The optimized TX and RX coils are fabricated and characterized individually to make them resonate at 13.56 MHz. The coil characterization are performed using Keysight E5061B vector network analyzer (VNA). The S-parameter file (SNP) extracted from the VNA are imported in Advance Design System (ADS) software by keysight. The Q-factor of the TX and RX coils are represented in Fig. 10(a). The Q-factor of the TX coils are found to be 113.6 and 74.8 at 13.56 MHz for the TX_1 and TX_2 , respectively. Although the TX coils are identical, the

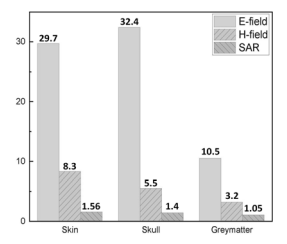


Fig. 11. Simulated E-field, H-field, and SAR values.

discrepancies are due to the precision of the fabrication and the low-conductivity solder that was used for the SMA connector integration.

The Q-factor of the proposed RX coil is measured to be 50 at 13.56 MHz. The RX coil is also simulated in HFSS and the simulation result shows the Q-factor value to be 80 at 13.56 MHz as illustrated in Fig. 10(a). The return loss of the TX coils are illustrated in Fig. 10(b) which shows a value of -9.7 and -10.3 dB for TX_1 and TX_2 , respectively, with a resonating capacitor of 82 pF in each of the TX coils. The simulated and measured result of RX coils shows that the return loss is -11.9and -10.5 dB, respectively at 13.56 MHz with a resonating capacitor of 864 pF. The return loss of the RX coil is measured for an optimum load resistance of 5.5 k Ω . As a result, a π -shape matching network is designed for matching the impedance of the PMU and the stimulation circuit with 5.5 k Ω . The π -shape CLC (Capacitor-Inductor-Capacitor) matching network is designed after the RX coil having the values of 2 pF capacitance and 1.3 nH inductance.

The proposed design is not surpassing the specific absorption rate (SAR) limit, regardless of the position of the on-chip PMU unit on top of a rat's head. The simulated E-field, H-field, and SAR values for the proposed TX and RX are represented in Fig. 11 when the input power to the TX antenna is 15 dBm. Here, the maximum SAR value is 1.56 W/kg which is below the FCC regulation. The maximum E-field through the skin layer is 32.4 V/m. A maximum H-field of 8.3 A/m is found through the skin layer. The TX and RX coils are coupled through inductive coupling and the PTE is defined by the power requirements of the PMU and stimulation circuit. Based on the power requirements of the PMU and stimulation circuit, the PTE of TX-RX coil is optimized. On the TX PCB board, sixteen positions are chosen based on the coordinates as shown in Fig. 6(a).

The theoretical maximum PTE of a WPT setup can be expressed in terms of the quality factors of the coils (Q_{TX} and Q_{RX}), and the coupling coefficient (k) as [30]:

$$PTE_{max} = \frac{k^2 Q_{TX} Q_{RX}}{(1 + \sqrt{1 + k^2 Q_{TX} Q_{RX}})^2}$$
 (5)

The coupling factor can be calculated as [31],

$$k = \frac{\mu_o N_1^2 r_1^2 A_2}{2L(d^2 + r_1^2)(3/2)} \tag{6}$$

Here, μ_o is the vacuum magnetic permeability, r_1 , N_1 are the transmitter inductor radius, number of wire loops, A_2 is the area of the receiver inductor and d the distance between the

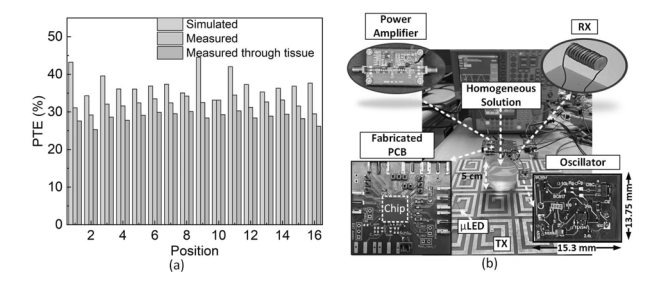


Fig. 12. (a) Simulated and measured PTE of the proposed WPT system. (b) Complete test-bench setup with detailed figure of the PCB boards.

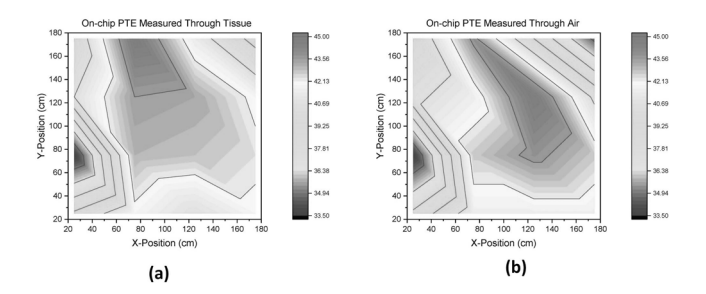


Fig. 13. (a) Measured PTE through tissue. (b) Measured PTE through air.

transmitter and receiver inductors. Using these equations, the maximum PTE from theoretical analysis is \sim 50%. The PTE values are simulated and measured at all of these positions with a separation of 6 cm between the TX and RX coils. The measured maximum PTE is \sim 35% at position 8 and the minimum value of the measured PTE is 28% at position 16. A homogeneous solution is created using NaCl, sugar, agar, benzoic acid (C6H5COOH), and water to emulate the brain tissue layers for the measurement through the tissue media. The sucrose based tissue-mimicking solution is designed according to the dielectric phantom recipe provided by the National Institute of Health (NIH) [32]. Fig. 12(a) also shows the measured PTE of the WPT system through 6 cm tissue solution where a maximum PTE of 30.3% is achieved at position 11. The testbench setup of the neuromodulation system is shown in Fig. 12(b) indicating the fabricated chip on PCB, TX coil, RX coil, PA, and oscillator board with μ LED. On-chip measured PTE in different locations through tissue and air is presented in Fig. 13(a) and (b).

C. Power Management Unit

The chip microphotgraph of the fabricated chip is represented in Fig. 15(a). The total dimension of the bare die is 2.25 mm \times 2.25 mm. The rectifier occupies 0.09 mm \times 0.3 mm area of the chip whereas the LDO circuit occupies 0.08 mm \times 0.1 mm area. The chip is packaged in 10 mm \times 10 mm Quad-flat-no lead (QFN) packages with 72 pins.

Fig. 14(a) shows the output voltages and currents with respect to various input voltages of the voltage doubler circuit derived from the post-layout simulation as well as measurements. The maximum output voltage of 4.1 V and output current of 7.3 mA is measured when the input voltage is 1 V and input current is 54 mA. The corresponding output power is 26 mW with a

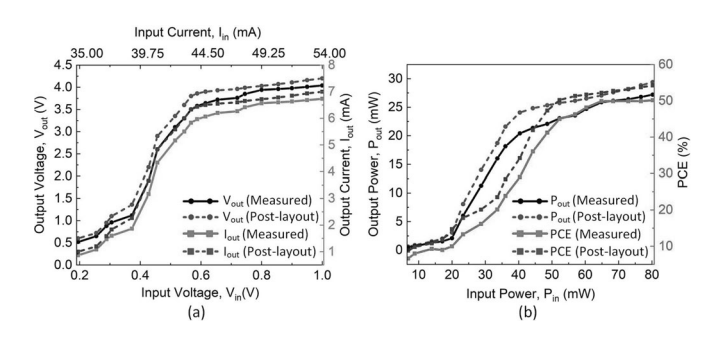


Fig. 14. (a) Measured output voltage and current of the seven-stage voltage doubler. (b) Measured output power and PCE of the voltage doubler.

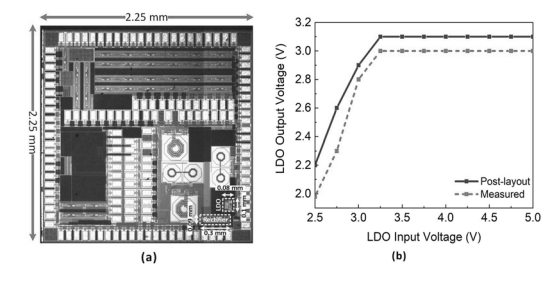


Fig. 15. (a) Chip microphotograph of the fabricated IC using 180 nm CMOS. (b) Output voltage and current of the LDO with respect to the varying input DC voltages.

maximum PCE of 52% for the maximum voltage output when the input power is 80 mW as shown in Fig. 14(b). The total PCE is defined as (7).

$$PCE(\%) = \frac{P_{outDC}}{P_{inAC}} \times 100\% \tag{7}$$

The output of the rectifier is fed through the LDO circuit to produce a constant voltage to the stimulation circuit. The LDO circuit is designed to provide an output of constant 3 V for an input voltage range of 3.1–7 V. As long as the input of the LDO circuit is above 3 V, the LDO circuit will be able to provide a constant 3 V to the stimulation circuit. Fig. 14(b) represents the post-layout simulation and measured output voltages of the LDO circuit. According to the measurement results, when the input voltage is above 3.2 V, the output voltage of the LDO is found to be 3 V.

To provide the minimum input voltage to the LDO from the voltage doubler, the required input voltage of the voltage doubler is 0.5 V, which results in a PCE of 22% and 13.5 mW DC power at the output of the rectifier.

D. Neural Stimulation Circuit

The output voltage of the LDO is used as the supply voltage for the MIC1555 oscillator which is used to achieve a reconfigurable pulse signal for stimulation. A fixed resistance is used as R_1 resistor while a variable resistor with a resistor value range from 10 to 110 k Ω is used as R_2 as shown in Fig. 9(a). The equivalent resistance of R_1 and R_2 helps to achieve the stimulation frequency range of 10 Hz to 50 Hz. For optogenetic neural stimulation, the suitable oscillation frequency is 10–80 Hz [34].

TABLE I
PERFORMANCE COMPARISON OF THE ON-CHIP RECTIFICATION CIRCUITRY
WITH THE STATE-OF-THE ARTS

Parameters	This work	[16]	[33]	
Process	180 nm	350 nm	130 nm	
Frequency	13.56 MHz	5 MHz	200 MHz	
Rectifier type	Voltage-doubler	Active-bridge	Diferential drive cross-coupled	
Input voltage	500 mV_{pp}	$3.2 V_{pp}$	$300 \text{ m}V_{pp}$	
Load resistance	3 kΩ	10 kΩ	32 kΩ	
PCE	52%	54%	70%	

TABLE II
PERFORMANCE COMPARISON OF THE WPT SYSTEM WITH THE STATE-OF-THE
ARTS

Parameters	This work	[20]	[35]	[36]	[37]	[38]
Frequency (MHz)	13.56	13.56	13.56	13.56	N/A	13.56
RX coil	3.4 mm ×	29 mm	10 mm ×	25 mm	60 mm	9.5
size	8 mm	diameter	10 mm	diameter	80 mm	diameter
Coil coupling	2-coil	4-coil	4-coil	5-coil	2-coil	3-coil
TX coil	215 mm ×	270 ×	10 mm ×	300 mm ×	200 mm ×	-
size	215 mm	270 mm	10 mm	300 mm	200 mm	
Distance	6 cm	4 cm	3-5 cm	7 cm	N/A	3 cm
Maximum	35	69	12.3	36.3	88.4	22.3
PTE (%),						

In cases of patients with Parkinson's disease, stimulation of the pedunculopontine nucleus between 20 and 45 Hz can improve sleep quality, cognition, and gait. At the start of treatment, stimulation of the globus pallidus internus at frequencies lower than 100 Hz has been beneficial for patients with dystonia. In certain cases of Parkinson's disease with freezing of gait and other axial symptoms, DBS at frequencies below 100 Hz is a therapeutic option [19]. In this work, a 20 Hz oscillation frequency with a voltage amplitude of 3 V is used to drive the μLED . Table II presents a comparison of the performances parameters of this work with the other state-of-the-art works. The proposed RX coil size is much smaller compared to the prior works. The PTE achieved by the proposed work is good enough to satisfy the power requirements of this work. Another comparison is represented in Table I for the on-chip circuitry which shows the architecture is able to achieve a similar PCE with lower load resistance compared to the state-of-the-art works.

IV. CONCLUSION

This article describes an optogenetic stimulation system that can stimulate neurons with reconfigurable light pulses. The system employs reconfigurable stimulation techniques, which enable it to record data for various optogenetic stimulation required for different brain regions. Off-chip components are used as prototypes. In the future, to make a fully implantable system, the stimulation circuit and the coil will also be integrated on-chip. The proposed system has a large footprint because of the off-chip components (LED driver, oscillator, etc.). In the future, every component will be integrated on-chip on a single die. As for now, we have used QFN packaging for testing the chip. After the bench-top verifications are completed, only the bare die (2.25 mm × 2.25 mm) on a flexible substrate will be implanted. Thus, the system can be made useful for neuromodulation applications in practical scenarios.

ACKNOWLEDGMENT

The authors would like to thank Travis Roberts for helping with the assembly of the system.

REFERENCES

- [1] J. Rivnay, H. Wang, L. Fenno, K. Deisseroth, and G. G. Malliaras, "Next-generation probes, particles, and proteins for neural interfacing," *Sci. Adv.*, vol. 3, no. 6, 2017, Art. no. e1601649.
- [2] S. M. Won, E. Song, J. T. Reeder, and J. A. Rogers, "Emerging modalities and implantable technologies for neuromodulation," *Cell*, vol. 181, no. 1, pp. 115–135, 2020.
- [3] J. Ausra et al., "Wireless, battery-free, subdermally implantable platforms for transcranial and long-range optogenetics in freely moving animals," *Proc. Nat. Acad. Sci.*, vol. 118, no. 30, 2021, Art. no. e2025775118.
- [4] Y. Yang et al., "Wireless multilateral devices for optogenetic studies of individual and social behaviors," *Nature Neurosci.*, vol. 24, no. 7, pp. 1035–1045, 2021.
- [5] I. R. Minev et al., "Electronic dura mater for long-term multimodal neural interfaces," *Science*, vol. 347, no. 6218, pp. 159–163, 2015.
- [6] A. Sridharan, S. D. Rajan, and J. Muthuswamy, "Long-term changes in the material properties of brain tissue at the implant–tissue interface," *J. Neural Eng.*, vol. 10, no. 6, 2013, Art. no. 066001.
- [7] X. Liu, Y. Lu, E. Iseri, Y. Shi, and D. Kuzum, "A compact closed-loop optogenetics system based on artifact-free transparent graphene electrodes," Front. Neurosci., vol. 12, 2018, Art. no. 132.
- [8] K. Matsushita et al., "A fully implantable wireless ECoG 128-channel recording device for human brain–machine interfaces: W-HERBS," Front. Neurosci., vol. 12, 2018, Art. no. 511.
- [9] P. Gutruf et al., "Wireless, battery-free, fully implantable multimodal and multisite pacemakers for applications in small animal models," *Nature Commun.*, vol. 10, no. 1, pp. 1–10, 2019.
- [10] A. Burton et al., "Wireless, battery-free subdermally implantable photometry systems for chronic recording of neural dynamics," *Proc. Nat. Acad. Sci.*, vol. 117, no. 6, pp. 2835–2845, 2020.
- [11] A. Basir and H. Yoo, "Efficient wireless power transfer system with a miniaturized quad-band implantable antenna for deep-body multitasking implants," *IEEE Trans. Microw. Theory Techn.*, vol. 68, no. 5, pp. 1943–1953, May 2020.
- [12] W.-C. Chen, C. W. L. Lee, A. Kiourti, and J. L. Volakis, "A multichannel passive brain implant for wireless neuropotential monitoring," *IEEE J. Electromagn.*, *RF, Microw. Med. Biol.*, vol. 2, no. 4, pp. 262–269, Dec. 2018.
- [13] U.-M. Jow, P. McMenamin, M. Kiani, J. R. Manns, and M. Ghovan-loo, "EnerCage: A smart experimental arena with scalable architecture for behavioral experiments," *IEEE Trans. Biomed. Eng.*, vol. 61, no. 1, pp. 139–148, Jan. 2014.
- [14] K. L. Montgomery et al., "Wirelessly powered, fully internal optogenetics for brain, spinal and peripheral circuits in mice," *Nature Methods*, vol. 12, no. 10, pp. 969–974, 2015.
- [15] S. Roy, R. J. -J. Roslee, M. T. Ahmed, and M. A. P. Mahmud, "Quad-band multiport rectenna for RF energy harvesting in ambient environment," *IEEE Access*, vol. 9, pp. 77464–77481, 2021.
- [16] T. Lehmann and Y. Moghe, "On-chip active power rectifiers for biomedical applications," in *Proc. IEEE Int. Symp. Circuits Syst.*, 2005, vol. 1, pp. 732– 735.
- [17] V. Stopjakova, M. Kovac, and M. Potocny, "On-chip energy harvesting for implantable medical devices," *Radioengineering*, vol. 29, no. 2, pp. 269–284, 2020.
- [18] A. M. Kuncel and W. M. Grill, "Selection of stimulus parameters for deep brain stimulation," *Clin. Neuriophysiol.*, vol. 115, no. 11, pp. 2431–2441, 2004
- [19] J. F. Baizabal-Carvallo and M. Alonso-Juarez, "Low-frequency deep brain stimulation for movement disorders," *Parkinsonism Related Disord.*, vol. 31, pp. 14–22, 2016.

- [20] S. A. Mirbozorgi, H. Bahrami, M. Sawan, and B. Gosselin, "A smart cage with uniform wireless power distribution in 3D for enabling long-term experiments with freely moving animals," *IEEE Trans. Biomed. Circuits Syst.*, vol. 10, no. 2, pp. 424–434, Apr. 2016.
- [21] Y. Jia, S. A. Mirbozorgi, P. Zhang, O. T. Inan, W. Li, and M. Ghovanloo, "A dual-band wireless power transmission system for evaluating mm-sized implants," *IEEE Trans. Biomed. Circuits Syst.*, vol. 13, no. 4, pp. 595–607, Aug. 2019.
- [22] S. A. Mirbozorgi, P. Yeon, and M. Ghovanloo, "Robust wireless power transmission to mm-sized free-floating distributed implants," *IEEE Trans. Biomed. Circuits Syst.*, vol. 11, no. 3, pp. 692–702, Jun. 2017.
- [23] D. K. Biswas, N. T. Tasneem, and I. Mahbub, "Optimization of miniaturized wireless power transfer system to maximize efficiency for implantable biomedical devices," in *Proc. IEEE Texas Symp. Wireless Microw. Circuits* Syst., 2019, pp. 1–6.
- [24] A. Gefen, N. Gefen, Q. Zhu, R. Raghupathi, and S. S. Margulies, "Age-dependent changes in material properties of the brain and braincase of the rat," *J. Neurotrauma*, vol. 20, no. 11, pp. 1163–1177, 2003.
- [25] D. K. Biswas, N. T. Tasneem, and I. Mahbub, "Effects of coaxial-lateral and coaxial-angular displacements on link efficiency of a wirelessly powered optogenetic implant: Design, modeling, and experimental validation," *IEEE J. Electromagn.*, RF, Microw. Med. Biol., vol. 3, no. 4, pp. 269–275, Dec. 2019.
- [26] R. Hinrichs. et al., "Sources of magnetic fields," Physics 132: What is an Electron? What is Light?, 2020.
- [27] N. T. Tasneem, S. R. Suri, and I. Mahbub, "A low-power CMOS voltage boosting rectifier for wireless power transfer applications," in *Proc. Texas* Symp. Wireless Microw. Circuits Syst., 2018, pp. 1–4.
- [28] R. Singh, J. A. Cooper, M. R. Melloch, T. Chow, and J. W. Palmour, "SiC power schottky and PiN diodes," *IEEE Trans. Electron Devices*, vol. 49, no. 4, pp. 665–672, Apr. 2002.
- [29] J. Yi, W.-H. Ki, and C.-Y. Tsui, "Analysis and design strategy of UHF micro-power CMOS rectifiers for micro-sensor and RFID applications," *IEEE Trans. Circuits Syst. I: Regular Papers*, vol. 54, no. 1, pp. 153–166, Jan. 2007.
- [30] J. Sampath, A. Alphones, and H. Shimasaki, "Coil design guidelines for high efficiency of wireless power transfer (WPT)," in *Proc. IEEE Region* 10 Conf., 2016, pp. 726–729.
- [31] R. Matias, B. Cunha, and R. Martins, "Modeling inductive coupling for wireless power transfer to integrated circuits," in *Proc. IEEE Wireless Power Transfer*, 2013, pp. 198–201.
- [32] N. B. Initiative, "BRAIN 2025, A scientific vision," 2014. [Online]. Available: http://www.braininitiative.nih.gov/2025/BRAIN2025.pdf
- [33] M. Potocny, V. Stopjakova, and M. Kovac, "Self Vth-compensating CMOS on-chip rectifier for inductively powered implantable medical devices," in *Proc. IEEE 21st Int. Symp. Des. Diagnostics Electron. Circuits Syst.*, 2018, pp. 158–161.
- [34] L. A. Gunaydin, O. Yizhar, A. Berndt, V. S. Sohal, K. Deisseroth, and P. Hegemann, "Ultrafast optogenetic control," *Nature Neurosci.*, vol. 13, no. 3, pp. 387–392, 2010.
- [35] E. Maghsoudloo, M. Rezaei, and B. Gosselin, "A wirelessly powered high-speed transceiver for high-density bidirectional neural interfaces," in *Proc. IEEE Int. Symp. Circuits Syst.*, 2017, pp. 1–4.
- [36] B. Lee, M. Kiani, and M. Ghovanloo, "A smart wirelessly powered homecage for long-term high-throughput behavioral experiments," *IEEE Sensors J.*, vol. 15, no. 9, pp. 4905–4916, Sep. 2015.
- [37] J. J. Casanova, Z. N. Low, J. Lin, and R. Tseng, "Transmitting coil achieving uniform magnetic field distribution for planar wireless power transfer system," in *Proc. IEEE Radio Wireless Symp.*, 2009, pp. 530–533.
- [38] A. Basir, I. A. Shah, and H. Yoo, "Sphere-shaped receiver coil for misalignment-resilient wireless power transfer systems for implantable devices," *IEEE Trans. Antennas Propag.*, vol. 70, no. 9, pp. 8368–8378, Sep. 2022.